JOURNAL OF COMPUTATIONAL PHYSICS 110, 134–149 (1994)

Arbitrary Domain Velocity Analyses for the Incompressible Navier–Stokes Equations

YAO-HSIN HWANG

Chung Shun Institute of Science and Technology, Lung Tan 90008-15-1, Taiwan 32526, Republic of China

Received June 1, 1992; revised March 15, 1993

This paper describes the development of a calculation procedure for fluid flow in arbitrary domains. This method is based on the finite-volume formulation in the arbitrary Lagrangian–Eulerian (ALE) grid. Coordinate transformation is not necessary and the physical geometrical quantities are directly applied. The derivations are obtained by the divergence theorem, and the diffusion terms in the governing equations on the control surfaces are represented by a two-point related gradient expression. A split velocity concept is employed to link the interferences of adjacent pressure nodes and eliminate the pressure wiggle problem. The total mass flux is kept unchanged in the split velocity field, as in the original velocity field determined from the momentum equations, which implies the consistency of the pressure correction process. Three typical test problems of flow in a gradual expansion duct, flow in a double bent channel, and natural convection between concentric and eccentric annuli have been calculated to indicate the feasibility and performances of the present formulation. Results showed that this method is a robust and efficient tool to determine the fluid flow characteristic and heat transfer process for problems with complicated boundaries.

1. INTRODUCTION

The orthogonal grid system applied in complex geometries to numerically solve the fluid flow problems will, in general, require special interpolation of boundary conditions due to the inconsistency of physical boundary and computational grid surface. This interpolation may induce computational errors and yield inaccurate prediction of the fluid flow. Therefore, the body-fitted coordinates or unstructured grid methods are adopted to avoid the complicated assignment of boundary conditions. In body-fitted coordinates, three types of grid system according to their relative computational positions of pressure and velocity variables are usually employed [1]. They are the staggered grid, the collocated grid, and the arbitrary Lagrangian–Eulerian (ALE) grid. In the staggered grid [2], pressure is defined at the computational grid node and velocity components are located midway between two adjacent pressure points. The staggered grid is proven to be quite robust and efficient in orthogonal grid computations. No further adjustment for pressure correction equation is needed, since the mass flux in the continuity equation derived from the discretized momentum equations reasonably corresponds to the pressure gradient across the control surface. Special treatments required by the momentum interpolation in the collocated grid [3] and required by the split velocity concept [4] in the ALE grid must be adopted to eliminate the checkerboard pressure field. However, in the case of the body-fitted coordinates, different computational locations for velocity components in the staggered grid may impose additional disadvantages, no matter which components of the velocity vector are chosen to be the dependent variables. If the Cartesian velocity components are selected to be the dependent variables, there may exist a pressure oscillation field when the grid lines rotate by 90° [5] and the mass flux across the control surface in the continuity equation needs further interpolation. The Cartesian velocity direction is fixed and the physical grid staggering direction may be changed to a large extent in general body-fitted coordinates and, therefore, the original advantages in grid staggering will be weakened. On the other hand, the choice of curvilinear velocity components, covariant or contravariant velocity [6, 7], does attenuate the drawback of adopting Cartesian velocity but the convection terms in momentum equations will no longer satisfy either the physical or the geometric conservation law form [8], since the linear momentum is conserved along a straight line not a curved line. The deterioration of conservation law form may cause numerical difficulties in the finite-volume formulation. Furthermore, it needs more mathematical manipulations and computational efforts to extend the staggered grid applied in advanced multigrid or unstructured grid methods.

The numerical difficulties due to the different computational positions of velocity components in the staggered grid can be avoided if the collocated or the ALE grid is adopted in complex geometries. In the collocated grid, all dependent variables are defined at the computational grid node and only one set of grid relations needs to be considered.

0021-9991/94 $6.00

However, as mentioned above, a momentum interpolation must be adopted to eliminate the checkerboard pressure field in the pressure correction procedure. Unfortunately, in this momentum interpolation, the velocities satisfying the momentum equation do not simultaneously satisfy the continuity equation. The total mass conservation may not be satisfied, although this discrepancy will be small in a refined grid. Meanwhile, a special treatment for pressure boundary condition must be considered, since the calculated pressure is also defined on the boundaries and will influence the fluid flow solution. Recently, Sotiropoulos and Abdallah [9] derived a new computational procedure using the collocated grid system such that the compatibility condition for the Poisson–Neumann problem will be automatically satisfied. However, the discrete continuity equation must be modified by adding an artificial source term. Similar treatment was also conducted by Lee and Tzong [10] in their APPLE or NAPPLE algorithm. In the ALE grid, pressure is defined at the computational node (scalar point) and all velocity components are located at the cell center (vector point). This grid arrangement can be regarded as a partially staggered grid, which is a compromise between the staggered and collocated grids, and the aforementioned individual inconveniences of the staggered and collocated grids may be alleviated. In fact, the ALE grid will be reduced to the staggered grid in the one-dimensional fluid flow case and to the collocated grid in the constant pressure situation.

Effects of grid staggering have been systematically studied by Shih *et al.* [11] who evaluated the performances of the above three grid systems and their modifications by comparing the individual shortcomings in 11 numerical and programming aspects. They showed that the ALE grid scheme is the best one in terms of "overall performance." However, they solved the derived pressure Poisson equation instead of the pressure correction equation and oscillatory pressure may subsequently occur as a numerical shortcoming. In order to eliminate the checkerboard pressure field in the ALE grid, Hwang [4] proposed a split velocity concept by using the pressure correction procedure in Cartesian coordinates. Using this concept, the velocity component in the X-direction, for instance, was split to north and south parts, according to the related pressure gradient effects across the control surface of the continuity equation. The split north or south velocity parts will contribute the mass fluxes on the east or west side of different but adjacent continuity control volumes. In this manner, the oscillatory pressure field was prevented and the total mass conservation was also satisfied. Hwang [4] also directly compared the performances of different grid sytems and he concluded that the required number of iterations for a converged solution for the ALE grid was competitive with that for the staggered grid.

The aim of this paper is to extend the split velocity concept for Cartesian coordinates to body-fitted coordinates. Contrary to previous derivations [3, 5, 7–9], coordinate transformation is not necessary; that is, the cumbersome geometric matrix of this partially staggered grid can be avoided. The physical volume, surface area, and other geometric quantities are directly derived in the physical plane. The Cartesian velocity vector is selected to be the dependent variable. The convection term is considered by its physical meaning as the projection of mass flux on the control surface. Diffusion terms and all quantities involving spatial gradients are represented by the nodal values by means of the divergence theorem [12]. Split velocities are derived so that the total mass flux is conserved, and the resulting flow solution is independent of the reference pressure level. Three typical flow situations were studied: flow in a gradual expansion duct, flow in a double rectangular bent channel, and natural convection in concentric and eccentric annuli. They were calculated to find the general performances of the present numerical scheme. Comparisons with other numerical results or experimental data were also performed. The calculated results show no oscillatory pressure field in the flow solutions. Reasonable agreements with other theoretical analyses or experimental data are also obtained. All the calculations and derivations in this paper are confined to structured two-dimensional grids; however, the present formulation can be easily extended to unstructured grid versions, since no coordinate transformation was needed.

2. MATHEMATICAL FORMULATION

2.1. *Governing Equations*

Consider the steady, laminar, incompressible Navier–Stokes equations expressed in the following generalized vector form:

$$\nabla \cdot (\rho \mathbf{V}\phi - \Gamma_\phi \nabla\phi) = S_\phi, \tag{1}$$

where $\mathbf{V}$ is the velocity vector and Γ_ϕ is the diffusion transport coefficient for variable ϕ. The terms in the LHS of Eq. (1) denote the convective transport term ($\rho \mathbf{V}\phi$) and diffusion transport term ($-\Gamma_\phi \nabla\phi$); S_ϕ is the remaining terms subtracted by convective and diffusive contribution and can be regarded as source term. Variable ϕ in Eq. (1) can be replaced by a physical quantity to represent its corresponding transport equation. If ϕ is replaced by one, then Eq. (1) represents the continuity equation, where both Γ_ϕ and S_ϕ vanish. For the X-direction momentum equation, ϕ in Eq. (1) can be substituted by the X-direction velocity component U; the diffusion transport coefficient and source term will be laminar viscosity (μ) and the X-direction pressure gradient ($-\partial P/\partial X$), respectively. Other transport equations can be determined in the same way, and Eq. (1)

will be referenced if necessary. In the pressure correction procedure, the continuity equation, instead of the explicit pressure governing equation, is solved to obtain the pressure distribution. However, pressure does not explicitly appear in the continuity equation and a relation between the corrected pressure and the velocity field must be derived. The essential parts of the present method is to derive such a relation and to eliminate the checkerboard pressure field produced by the standard pressure correction scheme [14] applied to the ALE grid system.

2.2. *Grid System*

As shown in Fig. 1, the pressure and other scalar dependent variables are defined at the computational grid node designated as the scalar point, and all the velocity components at the cell center which is designated as the vector point, since the velocity belongs to one of the vector quantities. In the present formulation, the derivation and calculated examples are confined to two dimensions to emphasize the essential ideas of this scheme, although the extension to three dimensions is quite straightforward. In Fig. 1, the location index (i, j) in logic space is also shown to represent the structured grid relation; however, this two-dimensional location index is not necessary, since the present derivation involves no coordinate transformation. The scalar points $(X_{i,j}, Y_{i,j})$ and the vector points $(X^v_{i,j}, Y^v_{i,j})$ are related as

$$\begin{aligned} X^v_{i,j} &= 0.25*(X_{i,j-1} + X_{i,j} + X_{i-1,j} + X_{i-1,j-1}) \\ Y^v_{i,j} &= 0.25*(Y_{i,j-1} + Y_{i,j} + Y_{i-1,j} + Y_{i-1,j-1}) \end{aligned} \tag{2}$$

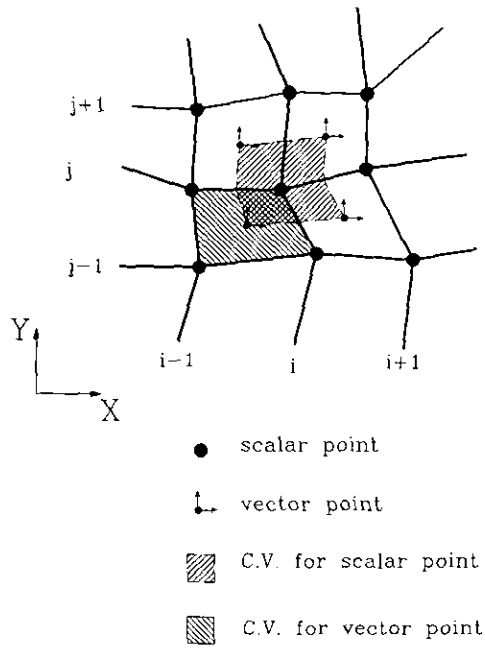

FIG. 1. Grid relation and control volumes in the ALE grid.

which implicitly defines the control volume of the vector point (i, j) to be the quadrilateral with the four scalar points $(i, j-1)$, (i, j), $(i-1, j)$, and $(i-1, j-1)$ as its vertices. This vector point control volume will be denoted the vector cell for convenience. The control volume for the dependent scalar variables in our ALE grid system is also shown in Fig. 1 and will be referred to as the scalar cell. The scalar cell is constructed by eight vertices including the four neighboring vector points and the four midpoints of the vector cell faces of $(i+1, j)$, $(i+1, j+1)$, $(i, j+1)$, and (i, j). Therefore, there are eight control faces for the scalar cell in contrast to the vector cell, which only consists of four control faces.

Using the grid system, the momentum equation is applied at a vector point and integrated over the vector cell. The continuity and energy equations (if needed) are applied at a scalar point and integrated over the scalar cell to form the finite difference equations. As mentioned above, no coordinate transformation is necessary, and the physical volume and surface area vector for the finite-volume formulation are directly derived from geometric relations;

$$\begin{aligned} \text{Vol} = 0.5*[&(X_3 - X_2)(Y_1 - Y_2) - (X_1 - X_2)(Y_3 - Y_2) \\ &+ (X_1 - X_4)(Y_3 - Y_4) - (X_3 - X_4)(Y_1 - Y_4)] \end{aligned} \tag{3}$$

for the volume of the quadrilateral enclosed by vertices 1, 2, 3, and 4 in counterclockwise order as shown in Fig. 2. The surface area vector (normal vector) from point 1 to point 2 in Fig. 2 may be derived as

$$\mathbf{A}_{1-2} = (Y_2 - Y_1)\,\mathbf{i} - (X_2 - X_1)\,\mathbf{j}. \tag{4}$$

The volume of the scalar cell will be the summation of those for four quadrilaterals as shown in Fig. 1. Furthermore, it should be noted that the grid arrangement in the present method is different from the original form of the ALE method [12], where the velocity components were defined at grid nodes and the pressure at cell centers.

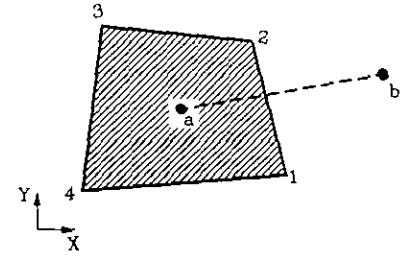

Volume=0.5*[(X3-X2)(Y1-Y2)-(X1-X2)(Y3-Y2)
+(X1-X4)(Y3-Y4)-(X3-X4)(Y1-Y4)]

Area(1-2)=(Y2-Y1)$\vec{i}$-(X2-X1)$\vec{j}$

FIG. 2. Representative control volume for geometric quantities.

2.3. *General Difference Procedure*

Using the finite-volume procedure, Eq. (1) is integrated over its control volume to deduce the corresponding finite difference equation at the specific computational location. Following the divergence theorem, the LHS of Eq. (1) becomes

$$\int_{cv} \nabla \cdot (\rho \mathbf{V}\phi - \Gamma_\phi \nabla\phi)\, d\mathbf{V} = \int_{cs} (\rho \mathbf{V}\phi - \Gamma_\phi \nabla\phi) \cdot d\mathbf{A}_n. \quad (5)$$

The finite difference equation can be obtained if Eq. (5) is further approximated as

$$\int_{cs} (\rho \mathbf{V}\phi - \Gamma_\phi \nabla\phi) \cdot d\mathbf{A}_n \to \sum_n (\rho \mathbf{V}\phi - \Gamma_\phi \nabla\phi)_n \cdot \mathbf{A}_n, \quad (6)$$

where subscript n denotes the control surface index, which must be counted over all control faces. For any specific face, Eq. (6) contains a convective and a diffusive contribution to the total flux across the control surface. The convective flux can be interpreted by its physical meaning as carrying the quantity ϕ by mass flow rate ($\rho \mathbf{V}$) across the control face. Consider the face 1–2 in Fig. 2 and the area vector in Eq. (4); the convective flux will be

$$(\rho \mathbf{V}\phi)_n \cdot \mathbf{A}_n = C_n \phi_n \quad (7a)$$

$$C_n = \rho[U_n(Y_2 - Y_1) - V_n(X_2 - X_1)], \quad (7b)$$

where C_n is the mass flow rate across the face. Subscript n now denotes the face from point 1 to point 2 in Fig. 2, and U, V are the velocity components in the X- and Y-directions, respectively. Equation (7b) for the mass flux can be verified to satisfy the geometric conservation law, since the sum of the mass fluxes on all the control surfaces will vanish in the constant velocity field [8]. The diffusion flux in Eq. (6) can be approximated by the simple formulas [15]:

$$(\Gamma_\phi \nabla\phi)_n \cdot \mathbf{A}_n = D_n(\phi_b - \phi_a) \quad (8a)$$

$$D_n = (\Gamma_\phi)_n [\mathbf{l}_{ba} \cdot \mathbf{A}_n / (\mathbf{l}_{ba} \cdot \mathbf{l}_{ba})]. \quad (8b)$$

In Fig. 2, the diffusion flux across the face 1–2 will be

$$D_n = (\Gamma_\phi)_n \frac{[(X_b - X_a)(Y_2 - Y_1) - (Y_b - Y_a)(X_2 - X_1)]}{[(X_b - X_a)^2 + (Y_b - Y_a)^2]}. \quad (8c)$$

The total flux through the control surface 1–2 in Fig. 2 can then be expressed by combining the convective and diffusive contributions [16],

$$F_n = D_n f(C_n/D_n)(\phi_b - \phi_a) + C_n \phi_{up}, \quad (9a)$$

where ϕ_{up} is the upwind value of ϕ,

$$\phi_{up} = 0.5*[(\phi_a + \phi_b) + (\phi_a - \phi_b)\, C_n/|C_n|], \quad (9b)$$

and $f(\ )$ is the scheme function [14] with the forms

$$\begin{aligned} &\text{center differences,} && f(\mathbf{P}) = 1 - 0.5*|\mathbf{P}| \\ &\text{upwind,} && f(\mathbf{P}) = 1 \\ &\text{hybrid,} && f(\mathbf{P}) = \text{Max}(0, 1 - 0.5*|\mathbf{P}|) \\ &\text{power law,} && f(\mathbf{P}) = \text{Max}(0, (1 - 0.1*|\mathbf{P}|)^5) \end{aligned} \quad (9c)$$

with the local cell Peclet number, $\mathbf{P} = C_n/D_n$. In the present study, the power law scheme is adopted, since it has been proven to be more accurate and stable in one dimension [14] for all cell Peclet numbers.

The volume integration of the source term in Eq. (1) can be treated in the same way if it contains spatial derivatives. For example, the source term in the X-direction equation involves the partial derivative of pressure with respect to $X(\partial P/\partial X)$, and its volume integration can be expressed as

$$\int_{cv} \left(\frac{\partial P}{\partial X}\right) d\mathbf{V} = \int_{cs} P\mathbf{i} \cdot d\mathbf{A}. \quad (10)$$

The finite difference expression can be obtained,

$$\int_{cs} P\mathbf{i} \cdot d\mathbf{A} \to \sum_n P_n A_{nx}, \quad (11)$$

where A_{nx} is the X-direction component of surface vector $\mathbf{A}_n$. For the surface 1–2 in Fig. 2, the pressure gradient contribution will be $P_n(Y_2 - Y_1)$.

Contributions of other control faces in Fig. 2 may also be accounted for in the same way as face 1–2, if the node numbering order is kept counterclockwise.

2.4. *Discretization of the Momentum Equations*

The discretized momentum equation at specific vector point (i, j) can be derived by integrating over the vector cell in Fig. 1. Using the general difference procedure described in Eqs. (5)–(11), the difference equation can be written on five-point form:

for the X-direction component,

$$a_p U_p = \sum_{nb} a_{nb} U_{nb} + S^u, \quad (12a)$$

for the Y-direction component,

$$a_p V_p = \sum_{nb} a_{nb} V_{nb} + S^v, \quad (12b)$$

with

$$a_p = \sum_{nb} a_{nb}, \tag{12c}$$

where the subscript p denotes the vector point index (i, j) and nb is the neighboring E, W, N, and S point; i.e., E denotes the east vector point $(i+1, j)$. It is noted that Eq. (12a) and Eq. (12b) only differ in the source term, because the control volume for U and V is the same. The vector cell face velocity in Eq. (7b) can be interpolated from its adjacent values. Therefore, the influence coefficients a_{nb} will be related to the convective and diffusive flux,

$$a_E = D_E \operatorname{Max}\left[0, \left(1 - 0.1^* \frac{|C_E|}{D_E}\right)^5\right] + \operatorname{Max}(0, -C_E) \tag{13a}$$

with

$$C_E = 0.5^* \rho^* [(U_{i+1,j} + U_{i,j})(Y_{i,j} - Y_{i-1,j}) - (V_{i+1,j} + V_{i,j})(X_{i,j} - X_{i-1,j})] \tag{13b}$$

$$D_E = (\Gamma_\phi)_E \frac{\left[\begin{array}{l}[(X^v_{i+1,j} - X^v_{i,j})(Y_{i,j} - Y_{i,j-1}) \\ \quad - (Y^v_{i+1,j} - Y^v_{i,j})(X_{i,j} - X_{i,j-1})]\end{array}\right]}{[(X^v_{i+1,j} - X^v_{i,j})^2 + (Y^v_{i+1,j} - Y^v_{i,j})^2]} \tag{13c}$$

for the east face. The other influence coefficients can be found in a similar fashion. In Eq. (13a), the power scheme was employed. Other schemes can be used just by modifying Eq. (13a) by the appropriate function described in Eq. (9c).

The source terms S^u and S^v in Eq. (12) can be determined if the pressure distribution along the edge of the vector cell is specified. In the present calculation, a linear distribution between two nodal pressures was assumed, and the resulting boundary pressure will be

$$P_E = 0.5^*(P_{i,j} + P_{i,j-1}) \tag{14}$$

for east face. Therefore, S^u and S^v can be found, if the overall contributions on the control surfaces are considered:

$$S^u = \tilde{b}^u_N P_{i,j} + \tilde{b}^u_W P_{i-1,j} + \tilde{b}^u_S P_{i-1,j-1} + \tilde{b}^u_E P_{i,j-1} \tag{15a}$$

and

$$S^v = \tilde{b}^v_N P_{i,j} + \tilde{b}^v_W P_{i-1,j} + \tilde{b}^v_S P_{i-1,j-1} + \tilde{b}^v_E P_{i,j-1} \tag{15b}$$

with

$$\begin{aligned} \tilde{b}^u_N &= -0.5^*(Y_{i-1,j} - Y_{i,j-1}) \\ \tilde{b}^u_W &= -0.5^*(Y_{i-1,j-1} - Y_{i,j}) \\ \tilde{b}^u_S &= -\tilde{b}^u_N \\ \tilde{b}^u_E &= -\tilde{b}^u_W \end{aligned} \tag{15c}$$

and

$$\begin{aligned} \tilde{b}^v_N &= 0.5^*(X_{i-1,j} - X_{i,j-1}) \\ \tilde{b}^v_W &= 0.5^*(X_{i-1,j-1} - X_{i,j}) \\ \tilde{b}^v_S &= -\tilde{b}^v_N \\ \tilde{b}^v_E &= -\tilde{b}^v_W. \end{aligned} \tag{15d}$$

It can easily be verified that the sum of all pressure influence coefficients ($\tilde{b}^u_{nb}$ and $\tilde{b}^v_{nb}$) in Eq. (15) will vanish. This implies that the difference equation and the resulting momentum equation will be independent of the reference pressure level, and the geometric conservation law for pressure gradient terms holds [8]. This is an important requirement of physical consistency in incompressible flow calculations.

2.5. *The Split Velocity Concept*

The velocity at a vector point can be determined from the discretized momentum equation (12), and this velocity field must also satisfy the continuity equation. Combining the source terms in Eq. (15) for the momentum equations, the X-direction difference momentum equation (12a) can be rearranged as

$$U_p = \tilde{U}_p + b^u_N P_{i,j} + b^u_W P_{i-1,j} + b^u_S P_{i-1,j-1} + b^u_E P_{i,j-1} \tag{16a}$$

with

$$\tilde{U}_p = \left(\sum_{nb} a_{nb} U_{nb}\right) \Big/ a_p \tag{16b}$$

$$b^u_{nb} = \tilde{b}^u_{nb}/a_p, \tag{16c}$$

where $\tilde{U}_p$ can be regarded as the pseudo-velocity of U_p which accounts for all terms in the RHS of the momentum difference equation, except the pressure gradient. The Y-direction difference equation can be handled in the same manner and, without loss of generality, will not be described here. Consider the vector cell at a specific location with node index (i, j) shown in Fig. 3. Since the vector cell is also composed in part by the four scalar cells $(i, j-1)$, (i, j), $(i-1, j)$, and $(i-1, j-1)$ in our ALE grid system, the velocity components U_e, U_n, U_w, and U_s in Fig. 3 will contribute to the mass flux through the control surfaces of those scalar cells. For example, U_e and U_n are two of the face velocities of scalar cell (i, j), whereas U_s and U_e will affect the scalar cell $(i, j-1)$ etc. If all the scalar cell face velocities are taken to be the same as the vector point velocity U in Fig. 3, then a linear interpolation between the adjacent vector point velocities prevails. A checkerboard pressure field may occur, although the velocity field from the discretized

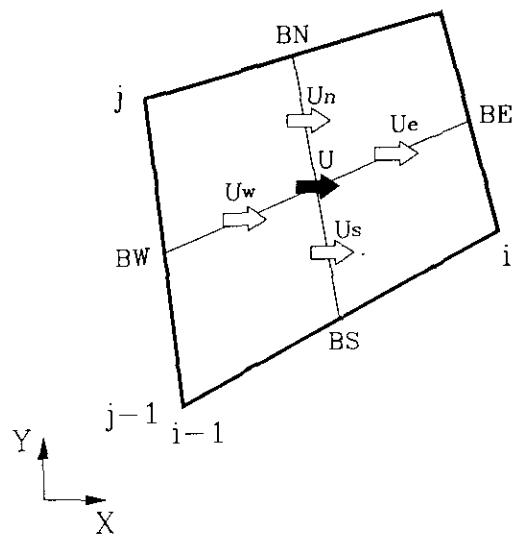

FIG. 3. Split velocities in vector cell.

momentum equations will fulfill the conservation of total mass flow rate [1]. However, the main purpose of this paper is to develop a pressure correction procedure without pressure wiggles, which calls for special treatment of the split velocities (U_e, U_n, U_w, and U_s). As can be seen from Eq. (16), the vector point velocity will be influenced by four neighboring pressure values which implies that the pressure gradient was evaluated at the vector point; however, the split velocity U_n should depend more on the pressure $P_{i,j}$ and $P_{i-1,j}$ than on $P_{i,j-1}$ and $P_{i-1,j-1}$, since the pressure gradient for a scalar cell face velocity should be evaluated at the midpoint of the grid line connecting the scalar points (i, j) and $(i-1, j)$, point BN in Fig. 3, for scalar cell (i, j). In fact, the influences of $P_{i,j-1}$ and $P_{i-1,j-1}$ vanish in Cartesian coordinates [4], and the split velocities U_n and U_s take the following form:

$$U_n = \tilde{U}_p + 2b^u_N P_{i,j} + 2b^u_W P_{i-1,j}$$
$$U_s = \tilde{U}_p + 2b^u_S P_{i-1,j-1} + 2b^u_E P_{i,j-1}.$$

However, the above split process must be modified in arbitrary grid coordinates, because the split velocity may depend on the reference pressure level and hence violate the physical consistency in incompressible flow calculations. For this reason, we propose a one-parameter split velocity group,

$$U_n = \tilde{U}_p + 2b^u_N P_{i,j} + 2b^u_W P_{i-1,j} - 2(b^u_N + 2b^u_W)\, P_c \quad (17a)$$
$$U_s = \tilde{U}_p + 2b^u_S P_{i-1,j-1} + 2b^u_E P_{i,j-1} - 2(b^u_S + 2b^u_E)\, P_c \quad (17b)$$

where P_c may be regarded as the grid-corrected pressure if the grid coordinate is not orthogonal. Prevailing a further observation on grid-corrected pressure and the physical meaning of pressure influence coefficients (b^u_{nb}) in Eq. (15), one may find that P_c will act on the line from BW to BE in Fig. 3 to influence the split velocities U_n and U_s. Therefore, the grid-corrected pressure P_c may be taken to be the vector point pressure.

$$P_c = 0.25*(P_{i,j} + P_{i-1,j} + P_{i-1,j-1} + P_{i,j-1}) \quad (18)$$

as the arithmetic average of adjacent nodal pressure. Consequently, the resulting split velocities will be

$$U_n = \tilde{U}_p + 2b^u_N P_{i,j} + 2b^u_W P_{i-1,j} - 0.5*(b^u_N + 2b^u_W) \times (P_{i,j} + P_{i-1,j} + P_{i-1,j-1} + P_{i,j-1}) \quad (19a)$$
$$U_s = \tilde{U}_p + 2b^u_S P_{i-1,j-1} + 2b^u_E P_{i,j-1} - 0.5*(b^u_S + 2b^u_E) \times (P_{i,j} + P_{i-1,j} + P_{i-1,j-1} + P_{i,j-1}). \quad (19b)$$

Similar expressions for the split velocities U_e and U_w can also be obtained:

$$U_e = \tilde{U}_p + 2b^u_N P_{i,j} + 2b^u_E P_{i,j-1} - 0.5*(b^u_N + 2b^u_E) \times (P_{i,j} + P_{i-1,j} + P_{i-1,j-1} + P_{i,j-1}) \quad (19c)$$
$$U_w = \tilde{U}_p + 2b^u_S P_{i-1,j-1} + 2b^u_W P_{i-1,j} - 0.5*(b^u_S + 2b^u_W) \times (P_{i,j} + P_{i-1,j} + P_{i-1,j-1} + P_{i,j-1}). \quad (19d)$$

In our grid system described in Section 2.2, the geometric relation in Fig. 3 clearly reveals that

$$Y^{BN} - Y^v_{i,j} = Y^v_{i,j} - Y^{BS} = 0.5*(Y^{BN} - Y^{BS}). \quad (20)$$

The split velocity in Eq. (19) also satisfies the relation

$$U_n + U_s = 2U_p. \quad (21)$$

Therefore, the total mass flux in the original vector point velocity field is kept unchanged as in the split velocity field, since the condition

$$U_p(Y^{BN} - Y^{BS}) = U_n(Y^{BN} - Y^v_{i,j}) + U_s(Y^v_{i,j} - Y^{BS}) \quad (22a)$$

holds which follows immediately from Eqs. (20) and (21). Equality of the mass flow rate between the split velocities and the vector point velocity on the EW line is also observed, since the following equation is satisfied:

$$U_p(Y^{BE} - Y^{BW}) = U_e(Y^{BE} - Y^v_{i,j}) + U_w(Y^v_{i,j} - Y^{BW}). \quad (22b)$$

As for the Y-direction component V, the above equations may be proven to be valid if the X-direction velocity U is

replaced by V, and the Y-coordinates by the X-coordinates. Using the velocity splitting procedure in Eqs. (17)–(19), the face velocities for the scalar cells will reasonably reflect the pressure gradient effects on the control surfaces. In the original ALE formulation for uniform grid distribution [12], one can prove that changes of pressure level at neighboring points, such as E, N, W, and S, will not affect the total mass flux across the control surfaces. There will exist two uncoupled networks of pressure points and an oscillatory pressure field may occur [1]. In fact, the present split velocity concept can be analog to the momentum interpolation in the collocated grid [3] in orthogonal coordinates. The mathematical and physical properties of the split velocity concept are briefly summarized:

1. The split velocities are independent of the reference pressure level;
2. The total mass flow rate in the split velocity field is kept unchanged as in the original vector point velocity field from discretized momentum equation;
3. A typical split velocity only depends on two adjacent nodal pressure values in Cartesian coordinates.

2.6. *Discretization of the Continuity Equation*

Since there are no diffusion or source terms involved in the continuity equation, only the discretized convection term has to be considered. As shown in Fig. 1, the control volume of the continuity equation (scalar cell) consists of four quadrilaterals and eight control surfaces. All convection fluxes on these eight faces must be taken into account. Figure 4 illustrates the X-direction face velocity more clearly. These face velocities are also the split velocities in the vector cell described in Section 2.5; for example, U_{wS} in Fig. 4 corresponds to U_n in Fig. 3, and U_{sW} to U_e in vector cell (i, j). Therefore, by applying Eq. (7) with $\phi \equiv 1$ to all control surfaces, the discretized continuity equation will be

$$C_{eS} + C_{eN} + C_{nE} + C_{nW} + C_{wN} + C_{wS} + C_{sW} + C_{sE} = 0 \tag{23}$$

with

$$C_{eS} = \rho[U_{eS}(Y^{BE} - Y^{v}_{i+1,j}) - V_{eS}(X^{BE} - X^{v}_{i+1,j})].$$

If the location index for split velocities is taken into account, then C_{eS} can be rewritten as

$$C_{eS} = \rho[(U_{i+1,j})_n (Y^{BE} - Y^{v}_{i+1,j}) - (V_{i+1,j})_n (X^{BE} - X^{v}_{i+1,j})], \tag{24}$$

where $(U_{i+1,j})_n$ and $(V_{i+1,j})_n$ represent the north split velocities in vector cell $(i+1, j)$ for the X- and Y-directions, respectively. The expressions for the other mass fluxes are similar to that of Eq. (24).

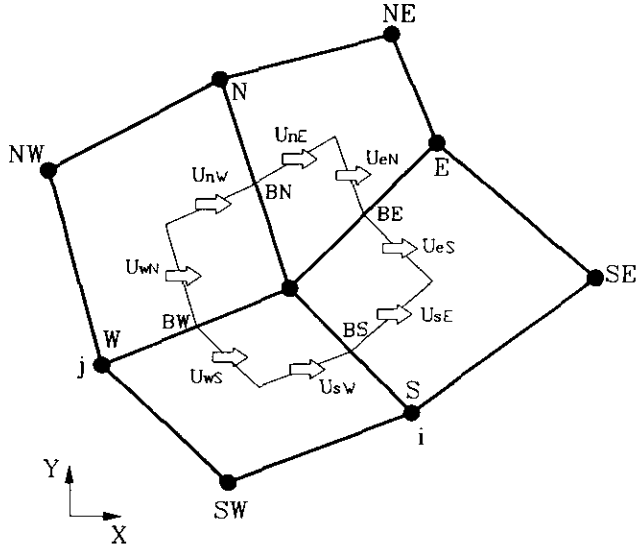

FIG. 4. Face velocities in scalar cell.

2.7. *Pressure Correction Procedure*

When the discretizations of the momentum and the continuity equations have been completed, a velocity–pressure correction relation must be employed to ensure that the velocity field satisfies all of the discretized equations. The pressure correction procedure of the SIMPLE [14] family serves this purpose. Although any revised SIMPLE scheme including SIMPLEC, SIMPLER, PISO, etc. can be used, the standard SIMPLE algorithm [14] is employed in this study for its simplicity. However, the resulting pressure correction equation applied to this generalized ALE grid will be different from that in the original SIMPLE algorithm, which was developed for orthogonal staggered grid systems. The essential ingredients of the present pressure correction process is described in the following paragraphs.

Let U^* and V^* denote the velocity components calculated from the discretized momentum equations (12). These velocities do not, in general, satisfy the discretized continuity equation (23) with the guessed pressure field P^*. These incorrect values (U^*, V^*, P^*) must be modified to the correct ones (U, V, P) through the following equations:

$$U = U^* + U', \qquad V = V^* + V', \qquad P = P^* + P'. \tag{25}$$

The fluctuating velocity components U' and V' should be related to the pressure P'. The variables in discretized velocity equation (16) are then substituted into Eq. (25), and a general but rather complicated correction relation between (U', V') and P' can be found. The SIMPLE algorithm simplifies this relation by setting the pseudo-velocity

and pressure influence coefficients in Eq. (16) fixed in the correction process, that is,

$$U'_p = b^u_N P'_{i,j} + b^u_W P'_{i-1,j} + b^u_S P'_{i-1,j-1} + b^u_E P'_{i,j-1}. \quad (26)$$

Similar correction relations for the split velocities in Eq. (19) can also be found:

$$U_n = U^*_n + U'_n, \qquad U_s = U^*_s + U'_s \quad (27a)$$

and

$$\begin{aligned} U'_n &= 2b^u_N P'_{i,j} + 2b^u_W P'_{i-1,j} - 0.5*(b^u_N + 2b^u_W) \\ &\quad \times (P'_{i,j} + P'_{i-1,j} + P'_{i-1,j-1} + P'_{i,j-1}) \\ U'_s &= 2b^u_S P'_{i-1,j-1} + 2b^u_E P'_{i,j-1} - 0.5*(b^u_S + 2b^u_E) \\ &\quad \times (P'_{i,j} + P'_{i-1,j} + P'_{i-1,j-1} + P'_{i,j-1}). \end{aligned} \quad (27b)$$

It is noted that the correction equations of the split velocities and the vector point velocity in Eqs. (27) and (26) are consistent, since the condition

$$U'_p = 0.5*(U'_n + U'_s) \quad (28)$$

automatically holds which implies that the correction for the mass flux in the discretized continuity equation and the momentum equations is also consistent.

The correction form for the discretized continuity equation (23) can then be found by substituting the fluctuating split velocities into Eq. (23),

$$C'_{eS} + C'_{eN} + C'_{nE} + C'_{nW} + C'_{wN} + C'_{wS} + C'_{sW} + C'_{sE} = -S_m \quad (29)$$

with

$$\begin{aligned} S_m &= C^*_{eS} + C^*_{eN} + C^*_{nE} + C^*_{nW} + C^*_{wN} + C^*_{wS} + C^*_{sW} + C^*_{sE} \\ C'_{eS} &= \rho[(U'_{i+1,j})_n (Y^{BE} - Y^v_{i+1,j}) \\ &\quad - (V'_{i+1,j})_n (X^{BE} - X^v_{i+1,j})], \end{aligned}$$

where S_m can be regarded as the mass flux error in the discretized continuity equation due to the velocity field from the discretized momentum equations. Substituting Eq. (27b) into Eq. (29), the difference pressure correction equation can then be found,

$$a_p P'_p = \sum a_{nb} P'_{nb} - S_m \quad (30)$$

with

$$\begin{aligned} a_E &= \rho[1.5*(b_{i+1,j})^v_N - 0.5*(b_{i+1,j})^v_W](X^{BE} - X^v_{i+1,j}) \\ &\quad - [1.5*(b_{i+1,j})^u_N - 0.5*(b_{i+1,j})^u_W](Y^{BE} - Y^v_{i+1,j}) \\ &\quad + [1.5*(b_{i+1,j+1})^v_E - 0.5*(b_{i+1,j+1})^v_S](X^v_{i+1,j+1} - X^{BE}) \\ &\quad - [1.5*(b_{i+1,j+1})^u_E - 0.5*(b_{i+1,j+1})^u_S](Y^v_{i+1,j+1} - Y^{BE}) \\ a_{NE} &= 0.5*\rho*[(b_{i+1,j+1})^u_E + (b_{i+1,j+1})^u_S](Y^v_{i+1,j+1} - Y^{BE}) \\ &\quad - 0.5*[(b_{i+1,j+1})^v_E + (b_{i+1,j+1})^v_S](X^v_{i+1,j+1} - X^{BE}) \\ &\quad + 0.5*[(b_{i+1,j+1})^u_S + (b_{i+1,j+1})^u_W](Y^{BN} - Y^v_{i+1,j+1}) \\ &\quad - 0.5*[(b_{i+1,j+1})^v_S + (b_{i+1,j+1})^v_W](X^{BN} - X^v_{i+1,j+1}) \\ a_p &= \sum_{nb} a_{nb}, \end{aligned}$$

where subscript *nb* denotes the eight neighboring points (*E*, *NE*, *N*, *NW*, *W*, *SW*, *S*, and *SE*); the superscripts *BE* and *BN* refer to the boundary points in Fig. 4. All other influence coefficient not shown in Eq. (30) can also be found by some simple algebraic operations.

3. SOLUTION PROCEDURE

The solution procedure in the SIMPLE algorithm is described by the following operations:

1. Guess the velocity and pressure field;
2. Solve the discretized momentum equations (12) to obtained the starred velocity field;
3. Calculate the split velocities from Eq. (19);
4. Solve the pressure condition equation (30) to find the corrective pressure field P';
5. Update the pressure field from Eq. (25) by adding P' to P^*;
6. Update the velocity field by the velocity correction equation (26);
7. Solve the other discretized equations for variable ϕ (if needed);
8. Take the corrected velocity and pressure field as a new guessed solution and return to step 2 until the criterion for convergence is satisfied.

The convergence criterion in this study is defined as the summation of mass flux and the momentum flux residuals in the whole domain divided by their reference values must be less than a preset quantity. The reference values are decided by the individual characteristic quantities, such as flow rate and momentum flux in the continuity and momentum equations, respectively.

For solution of the algebraic equations originating from the discretized equations, the Thomas algorithm was iteratively applied line by line to solve the five-point related equations arising from the momentum equations, whereas a

modified strongly implicit procedure [17] was employed to solve the nine-point related pressure correction equation. The variables are underrelaxed between two successive calculations for numerical stability. The underrelaxation factors for velocity and pressure were assigned to be 0.8 and 0.2, respectively; they have been proven to be efficient in Cartesian ALE grid calculations [4].

4. APPLICATIONS

The computational procedure was applied to solve three test problems. They included: the fow in a gradual expansion duct, flow in a double bent channel, and natural convection in concentric and eccentric annuli. The governing equations for the first two cases, which are simple fluid flow problems, are the same as those described in Section 2.1, whereas those for the natural convection problem need an additional energy equation and modifications of the momentum equations, which will be discussed in later sections. For all these test problems, the flow geometries, boundary conditions, grid arrangements and calculated results will be presented in the following sections.

4.1. *Flow in a Gradual Expansion Duct*

The gradual expansion duct flow was a test problem for the workshop of IAHR on refined modeling [18]. Over 15 groups submitted their results on this problem and compared with those obtained by Cliff *et al.* [19] with finite element formulation, which was selected to be the benchmark solution since it has been proved to be grid independent. The geometry of this expansion duct, depicted in Fig. 5a, depends on the value of Reynolds number. The duct becomes longer and straighter as Re increases, and two different Re of 10 and 100 were studied in this paper. The lower boundary (solid wall) of the duct is given by the expression

$$YL(X) = [\tanh(2 - 30X/\mathrm{Re}) - \tanh(2)]/2 \quad \text{for} \quad 0 < X < X_{\text{out}} = \mathrm{Re}/3. \tag{31}$$

The upper boundary (symmetry plane) is located at $YU(X) = 1.0$. The inlet boundary conditions at $X = 0$ are given in terms of Cartesian velocity components U, V as

$$U = 3(Y - Y^2/2); \qquad V = 0 \qquad \text{for} \quad 0 < Y < 1.0 \tag{32}$$

which represents a fully developed channel velocity profile. The outflow boundary conditions at $X = \mathrm{Re}/3$ are specified as the extrapolated values from its interior point for all dependent variables except for the pressure, which is not necessary due to the grid staggering effect. Figure 5b represents the grid system adopted for Re = 10 in the physical plane. In this grid, a 42×42 uniform grid mesh was used in the following transferred plane:

$$\xi = X; \qquad \eta = [Y - YL(X)]/[YU(X) - YL(X)]. \tag{33}$$

This grid system was also adopted for Re = 100. The convergence histories for this test problem for Re = 10 and Re = 100 are illustrated in Figs. 6a, b. It is clear that the oscillatory residuals are confined to the initial stage and that the solutions converge after a certain number of iterations. Calculated results of pressure distributions on the lower wall, together with other numerical results, are presented in Figs. 7a, b for Re = 10 and Re = 100, respectively. The results of Demirovic and Gosman shown in Ref. [19] were obtained by a finite difference method and those of Karki and Patankar [20], by a finite volume procedure. As shown in Figs. 7a, b, the present predictions agree well with the

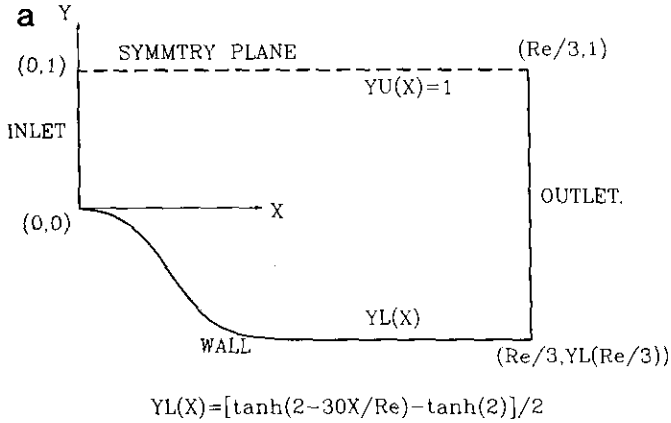

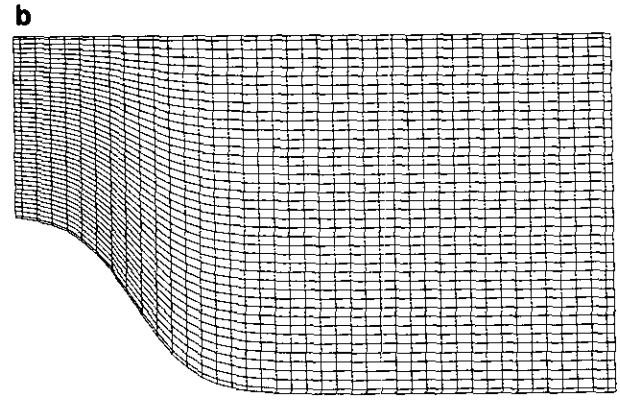

FIG. 5. Flow in a gradual expansion duct: (a) geometry; (b) grid system.

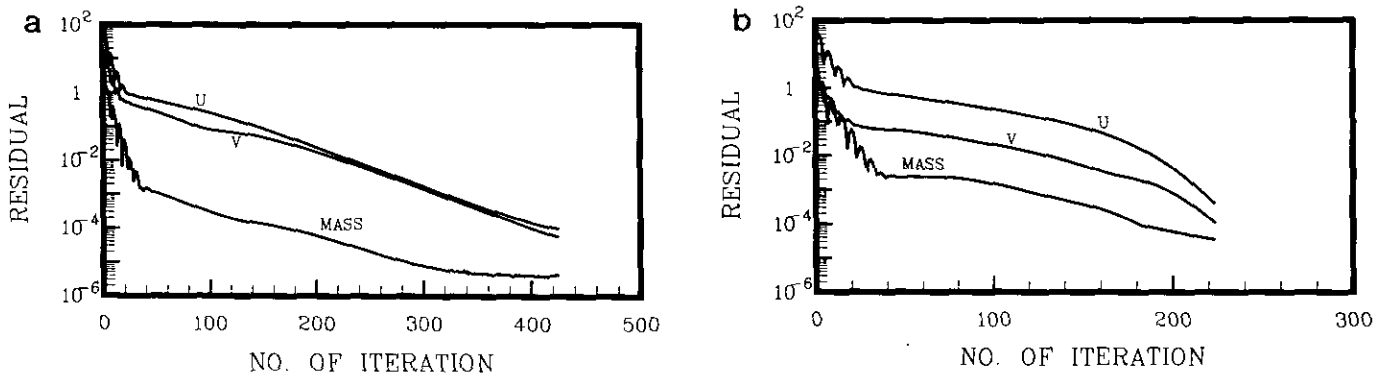

FIG. 6. Convergence histories for flow in a gradual expansion duct: (a) Re = 10; (b) Re = 100.

other numerical results. The qualitative trend predicted by the present method also follows the benchmark solution for Re = 10 near the channel inlets. Figures 8a, b show the corresponding pressure field for Re = 10 and Re = 100, respectively. It can be seen that the pressure fields are very smooth and that the oscillatory pressure does not occur by the present method.

4.2. *Flow in a Double Bent Channel*

The corrugated wall has been designed to be effective for enhancing the heat transfer rate in the channel. The flowfield will consist of the complicated flow impingement, separation, and reattachment characteristics in a double bent channel. In this section, the fluid flow characteristics are considered, and the temperature effects on the fluid properties are assumed to be negligible. Figure 9 shows the geometry and an 82×12 grid arrangement for a typical double bent channel, where the channel step ratio is three. This channel flow has been experimentally studied by Izumi *et al.* [21] using a flow visualization technique and numerically analyzed by Amano [22], who adopted the modified TEACH code on a 54×36 Cartesian grid system to cover the computational domain. A large portion of up to 60–70% of the grid points lying outside the computational boundary have been wasted in Amano's analysis. Therefore, the number of effective grid points in the present study is higher than those in Amano's analysis. Figure 10 shows the convergence history for this test problem in the present study. Less than 70 iterations were executed to satisfy the convergence criterion when the momentum and continuity residual was less than 5×10^{-4}; however, Amano reported that more than 200 iterations were needed to satisfy the convergence criterion of 1.5×10^{-2} in his modified TEACH-based scheme. The average central processor time for the converged solution reported by Amano [22] was about 5 min on a UNIVAC 1100, whereas, in the present analysis, the required CPU time was about 2 min on a HP7200 Workstation. The calculated streamwise velocity profiles, streamlines, and pressure contour are depicted in Figs. 11a, b, c, respectively. The streamwise velocity profile is similar to those in Amano's analysis [22], and the streamlines qualitatively agree with the observations by Izumi *et al.* [21]. Furthermore, Izumi *et al.* [21] estimated the corner pressure value at the second bend on the lower wall to be approximately −3, and confirmed the pressure contours in Fig. 11c of the present results.

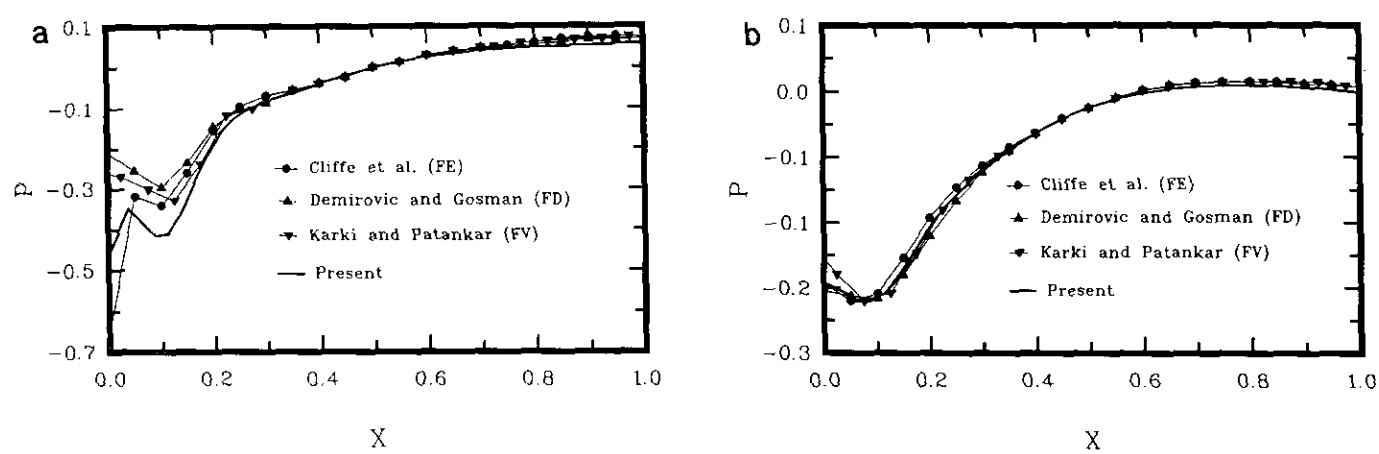

FIG. 7. Pressure distributions on lower wall for flow in a gradual expansion duct: (a) Re = 10; (b) Re = 100.

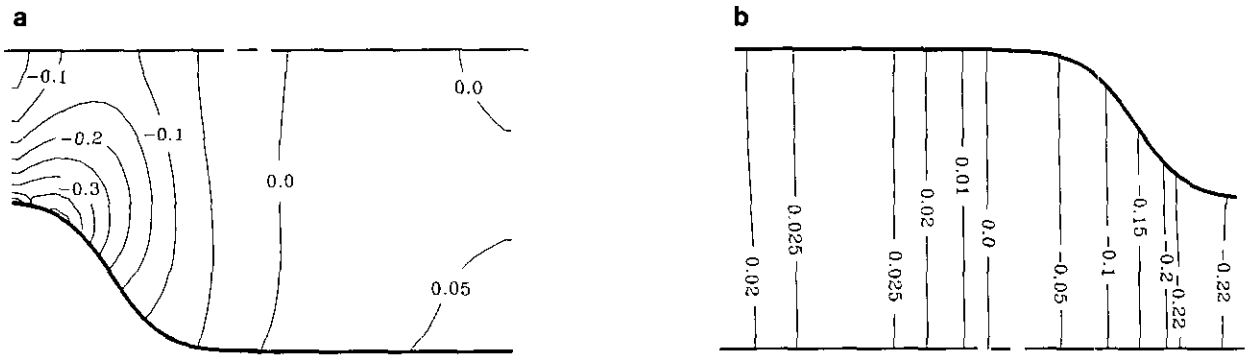

FIG. 8. Calculated pressure field for flow in a gradual expansion duct: (a) Re = 10; (b) Re = 100.

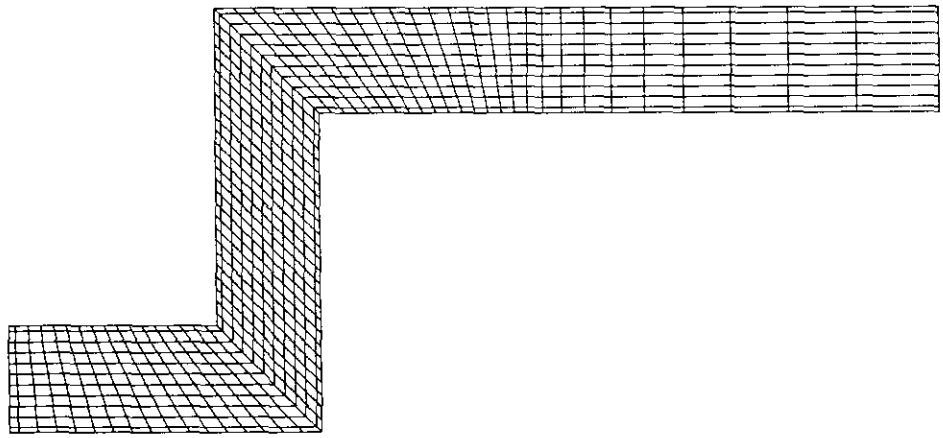

FIG. 9. Geometry and grid system for a double bent channel.

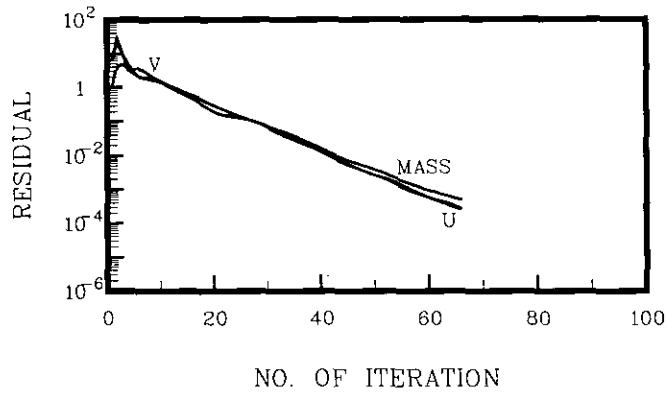

FIG. 10. Convergence history for flow in a double bent channel.

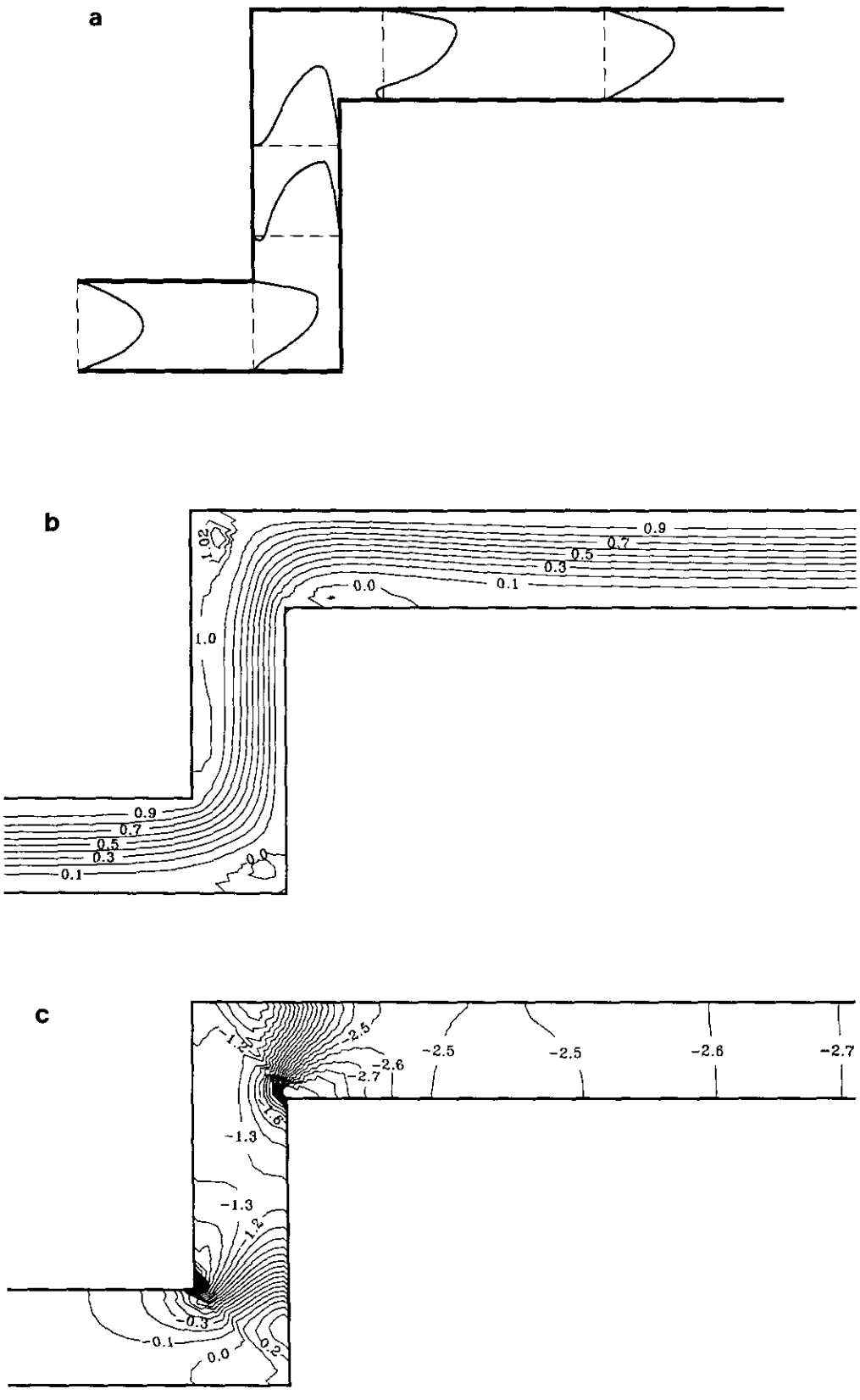

FIG. 11. Calculated results for flow in a double bent channel: (a) streamwise velocity profiles; (b) streamlines; (c) pressure.

4.3. *Natural Convection in Concentric and Eccentric Annuli*

Natural convection heat transfer in horizontal annuli involves complicated interactions between hydrodynamics and thermal effects. Kuehn and Goldstein [23] experimentally studied these phenomena by a Mach–Zehnder interferometer to determine the temperature distributions and local heat transfer coefficients. Projahn *et al.* [24] performed a stream-vorticity formulation to numerically analyze the fluid flow and heat transfer process. These experimental and theoretical results are used to check the present predictions. The schematic diagram of the problem and the corresponding computational grid system are depicted in Figs. 12a, b. The 62×22 grid was assigned to be uniformly distributed both in THETA-r, where r is defined as

$$r = (R - R_i)/(R^* - R_i) \tag{34}$$
$$R^* = -E_v \cos(\text{THETA}) + [R_o^2 - E_v^2 \sin^2(\text{THETA})]^{1/2};$$

that is, $r = 0$ for the inner wall and $r = 1$ for the outer wall.

As mentioned above, the governing equations described in Section 2.1 must be modified, and an additional energy equation must be solved to determine the temperature distribution in this natural convection problem. If the nondimensional variables are defined as

$$\begin{aligned} x &= X/L; & y &= Y/L \\ u &= UL/\alpha; & V &= VL/\alpha \\ \theta &= (T - T_o)/(T_i - T_o); & p &= PL^2/\rho\alpha^2 \\ \text{Ra} &= \frac{g\beta(T_i - T_o)L^3}{\nu\alpha}; & \text{Pr} &= \nu/\alpha, \end{aligned} \tag{35}$$

where g is the acceleration of gravity, α is the thermal diffusivity, β is the fluid expansion coefficient, ν is the kinematic viscosity, and L is the radius difference between two cylinders:

$$L = R_o - R_i. \tag{36}$$

In our calculation, the same geometry of Kuehn and Goldstein [23] with $L/R_i = 1.6$ was chosen. The dimensionless governing equations will be

$$\frac{\partial}{\partial x}(u) + \frac{\partial}{\partial y}(v) = 0$$
$$\left[\frac{\partial}{\partial x}\left(uu - \frac{\partial u}{\partial x}\right) + \frac{\partial}{\partial y}\left(vu - \frac{\partial u}{\partial y}\right)\right] \Big/ \text{Pr} = -\frac{\partial p}{\partial x} + \text{Ra}\,\theta \tag{37}$$
$$\left[\frac{\partial}{\partial x}\left(uv - \frac{\partial v}{\partial x}\right) + \frac{\partial}{\partial y}\left(vv - \frac{\partial v}{\partial y}\right)\right] \Big/ \text{Pr} = -\frac{\partial p}{\partial y}.$$

The Boussinesq approximation in density has been assumed in the above governing equations. The boundary conditions are:

$$\begin{aligned} &u = v = 0, \quad \theta = 1 && \text{for} \quad r = 0 && \text{(inner wall)} \\ &u = v = \theta = 0 && \text{for} \quad r = 1 && \text{(outer wall)} \\ &v = \frac{\partial u}{\partial y} = \frac{\partial \theta}{\partial y} = 0 && \text{symmetry plane(THETA} = 0^\circ \text{ or } 180^\circ\text{)}. \end{aligned} \tag{38}$$

Three concentric and eccentric cases of ($E_v = 0$, $\text{Ra} = 5 \times 10^4$), ($E_v = -0.625$, $\text{Ra} = 5 \times 10^4$) and ($E_v = 0.652$,

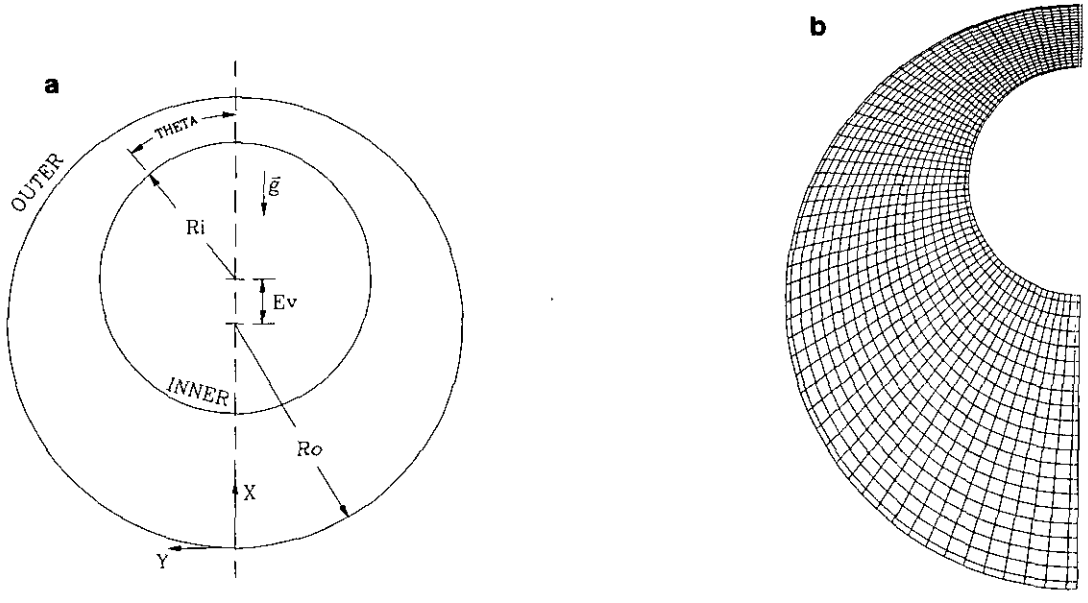

FIG. 12. Natural convection in concentric and eccentric annuli: (a) geometry; (b) grid system.

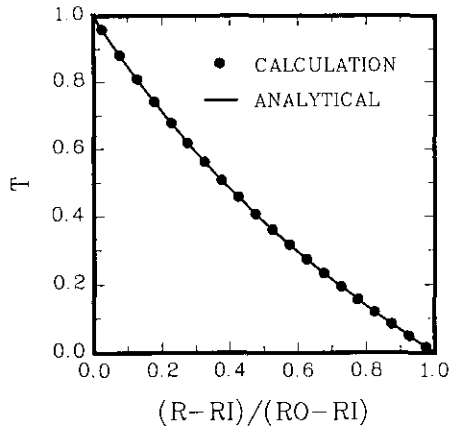

FIG. 13. Calculated and analytical temperature distributions for pure conduction in concentric annuli.

$Ra = 4.8 \times 10^4$) were calculated to directly compare the results of Kuehn and Goldstein [23] and Projahn *et al.* [24]. Before the interaction between the fluid flow and heat transfer processes has been investigated in natural convection, a ideal conduction in concentric annuli, where the analytical expression for the temperature distribution can be easily obtained, was calculated by the present procedure. As for the governing equations in Eq. (37), only the temperature transport equation without fluid flow effects was solved. Figure 13 illustrates the dimensionless temperature distribution of the calculated and the analytical results. The calculated results agree well with the analytical distribution in this pure conduction situation. Local equivalent conductivity on inner and outer walls of natural convection predictions are represented in Figs. 14a–c, together with other experimental and numerical results. The local equivalent conductivity is defined as

$$\begin{aligned} K &= h_i R_i \ln(R_o/R_i) \qquad \text{for the inner wall} \\ K &= h_o R_o \ln(R_o/R_i) \qquad \text{for the outer wall,} \end{aligned} \tag{39}$$

where h_i and h_o are the local heat transfer coefficients at the inner and outer cylinders, respectively. These heat transfer coefficients are based on the temperature difference between the two cylinders. It is evident from Figs. 14a–c that the present results agree with experimental data and other numerical results, except in the region of THETA < 30° at the outer cylinder for $E_v = 0.652$, where both numerical methods underestimate the heat transfer rate. Physically, the drop in heat transfer rate in this region is due to the occurrence of the second cavity near THETA = 0°. This phenomenon implies stronger interaction between fluid flow and heat transfer and is very critical for numerical predictions. Karki

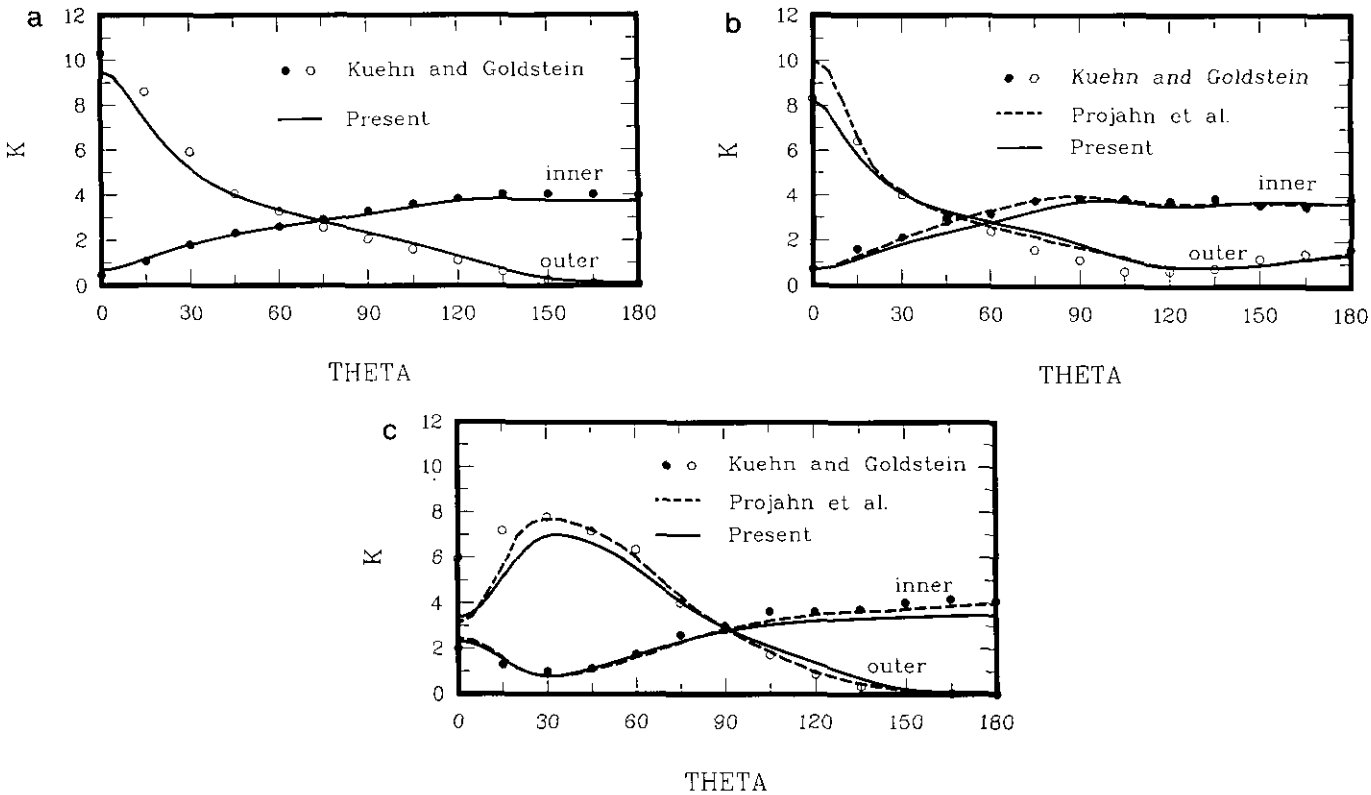

FIG. 14. Distributions of local equivalent conductivity for natural convection in concentric and eccentric annuli: (a) $E_v = 0.0$, $Ra = 5 \times 10^4$; (b) $E_v = -0.625$, $Ra = 5 \times 10^4$; (c) $E_v = 0.652$, $Ra = 4.8 \times 10^4$.

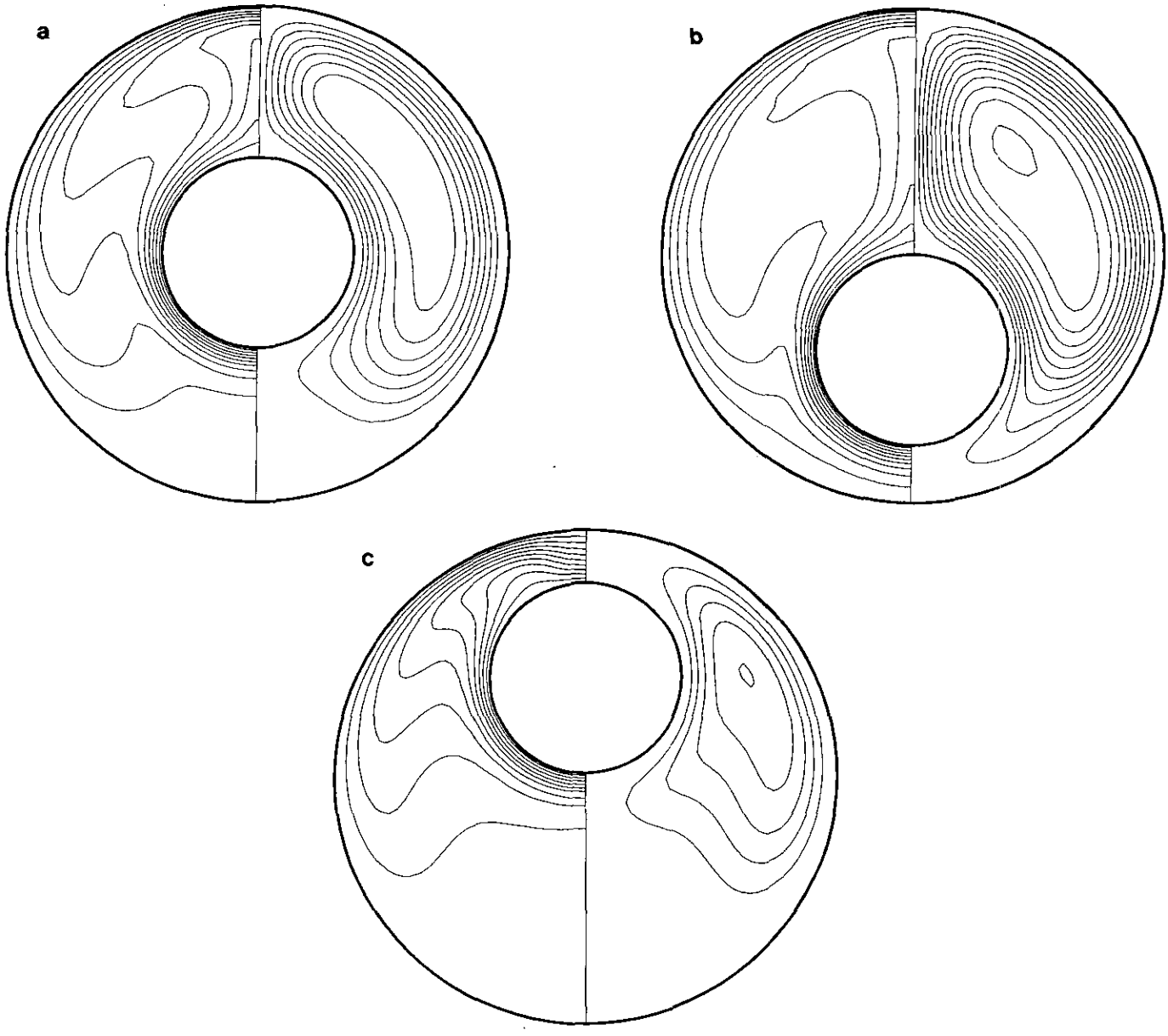

FIG. 15. Isotherms and streamlines for natural convection in concentric and eccentric annuli: (a) $E_v = 0.0$, $\mathrm{Ra} = 5 \times 10^4$; (b) $E_v = -0.625$, $\mathrm{Ra} = 5 \times 10^4$; (c) $E_v = 0.652$, $\mathrm{Ra} = 4.8 \times 10^4$.

and Patankar [20] speculated that the pronounced discrepancies between computational and experimental results were due to the inconsistency between the numerically and experimentally realized boundary conditions. The isotherms and streamlines for these three cases are shown in Figs. 15a–c. The distributions of local equivalent conductivity can be further interpolated by these figures. It is found that the inner cylinder is always surrounded by a thermal boundary layer, whereas the thermal boundary layer on the bottom portion of the outer cylinder does not exist for the case of positive eccentricity in Fig. 15c. This observation coincides with the experimental results of Kuehn and Goldstein [23]. Negative eccentricity increases the strength of the buoyancy-induced mass flow rate between the annuli and, on the contrary, positive eccentricity has the opposed effect. This is why the overall heat transfer rate is increased for negative eccentricity and decreased for positive eccentricity, which was observed by Kuehn and Goldstein [23].

5. CONCLUSIONS

The present work successfully derives a numerical method that is capable of analyzing fluid flow in irregular

geometries. This method employed the ALE grid which avoids the critical selection of velocity variables in fully staggered grids and the assignment of a pressure boundary condition in collocated grids. From the derivation procedure and computational results several conclsions can be drawn:

(1) Coordinate transformations are avoided in treating complicated boundaries and, therefore, the present method can be easily applied to unstructured grid arrangements.

(2) The present split velocity concept was proven to eliminate the pressure checkerboard field in body-fitted coordinates.

(3) The present formulation is quite efficient in terms of the convergence histories and required CPU time of test problems.

REFERENCES

1. R. Peyret and T. D. Taylor, *Computational Methods for Fluid Flow* (Springer-Verlag, New York, 1983).
2. F. H. Harlow and J. E. Welch, *Phys. Fluids* **8**, No. 12, 2182 (1965).
3. C. M. Rhie and W. L. Chow, *AIAA J.* **21**, No. 11, 1525 (1983).
4. Y. H. Hwang, *Numer. Heat Transfer B* **23**, 237 (1993).
5. W. Shyy, S. S. Tong, and S. M. Correa, *Numer. Heat Transfer* **8**, 99 (1985).
6. K. C. Karki and S. V. Patankar, *Numer. Heat Transfer* **14**, 295 (1988).
7. D. S. Joshi and S. P. Vanka, *Numer. Heat Transfer B* **20**, 61 (1991).
8. W. Shyy and T. H. Vu, *J. Comput. Phys.* **92**, 82 (1991).
9. R. Sotiropoulos and S. Abdallah, *J. Comput. Phys.* **103**, 336 (1992).
10. S. L. Lee and R. Y. Tzong, *Int. J. Heat Mass Transfer* **35**, No. 10, 2705 (1992).
11. T. M. Shih, C. H. Tan, and B. C. Hwang, *Int. J. Numer. Methods Fluids* **9**, 193 (1989).
12. C. W. Hirt, A. A. Amsden, and J. L. Cook, *J. Comput. Phys.* **14**, No. 3, 227 (1974).
13. Deleted in proof.
14. S. V. Patankar, *Numerical Heat Transfer and Fluid Flow* (McGraw–Hill, New York, 1980).
15. A. A. Amsden, J. D. Ramshaw, P. J. O'Rourke, and J. K. Dukowicz, "KIVA: A Computer Program for Two- and Three-Dimensional Fluid Flows with Chemical Reactions and Fuel Sprays," LA-10245-MS, 1985 (unpublished).
16. N. Taniguchi and T. Kobayashi, *Computer and Fluids* **19**, No. 3/4, 287 (1991).
17. G. E. Schneider and M. Zedan, *Numer. Heat Transfer* **4**, 1 (1981).
18. M. Napolitano and P. Orlandi, *Int. J. Numer. Methods Fluids* **5**, 667 (1985).
19. K. A. Cliffe, C. P. Jackson, and A. C. Greenfield, "Finite Element Solutions for Flow in a Symmetric Channel with a Smooth Expansion," AERE-R. 10608, 1983 (unpublished).
20. K. C. Karki and S. V. Patankar, *Numer. Heat Transfer* **14**, 309 (1988).
21. R. Izumi, K. Oyakawa, S. Kaga, and H. Yamashita, *J. Jpn. Soc. Mech. Eng.* **47**, No. 41b, 659 (1981).
22. R. S. Amano, *J. Heat Transfer* **106**, 591 (1984).
23. T. H. Kuehn and R. J. Goldstein, *J. Heat Transfer* **100**, 635 (1978).
23. U. Projahn, H. Reiger, and H. Beer, *Numer. Heat Transfer* **4**, 131 (1981).